28. L. M. Pazos-Outón *et al.*, *Science* **351**, 1430–1433 (2016).
29. M. Saba *et al.*, *Nat. Commun.* **5**, 5049 (2014).
30. C. Wehrenfennig, M. Liu, H. J. Snaith, M. B. Johnston, L. M. Herz, *J. Phys. Chem. Lett.* **5**, 1300–1306 (2014).
31. K. Chen, A. J. Barker, F. L. C. Morgan, J. E. Halpert, J. M. Hodgkiss, *J. Phys. Chem. Lett.* **6**, 153–158 (2015).
32. J. M. Frost, A. Walsh, *Acc. Chem. Res.* **49**, 528–535 (2016).
33. R. Righini, *Science* **262**, 1386–1390 (1993).
34. P. Foggi, R. Righini, R. Torre, L. Angeloni, S. Califano, *J. Chem. Phys.* **96**, 110–115 (1992).
35. M. T. Weller, O. J. Weber, J. M. Frost, A. Walsh, *Phys. Chem. Lett.* **6**, 3209–3212 (2015).
36. A. A. Bakulin *et al.*, *J. Phys. Chem. Lett.* **6**, 3663–3669 (2015).
37. N. Balkan, *Hot Electrons in Semiconductors* (Oxford Univ. Press, 1998).
38. A. J. Nozik, *Annu. Rev. Phys. Chem.* **52**, 193–231 (2001).
39. U. Bockelmann, G. Bastard, *Phys. Rev. B Condens. Matter* **42**, 8947–8951 (1990).
40. Y. Yang *et al.*, *Nat. Photonics* **10**, 53–59 (2016).
41. M. B. Price *et al.*, *Nat. Commun.* **6**, 8420 (2015).
42. L. Landau, *Phys. Z. Sowjetunion* **3**, 664 (1933).
43. G. R. Berdiyorov *et al.*, *J. Phys. Chem. C* **120**, 16259–16270 (2016).
44. Y. J. Chang, E. W. Castner, *J. Chem. Phys.* **99**, 7289–7299 (1993).
45. Y. Zhou *et al.*, *Nat. Commun.* **7**, 11193 (2016).
46. A. Pecchia, D. Gentilini, D. Rossi, M. Auf der Maur, A. Di Carlo, *Nano Lett.* **16**, 988–992 (2016).
47. C. Quarti, E. Mosconi, F. De Angelis, *Phys. Chem. Chem. Phys.* **17**, 9394–9409 (2015).
48. S. A. March *et al.*, https://arxiv.org/abs/1602.05186 (2016).
49. R. T. Ross, A. J. Nozik, *J. Appl. Phys.* **53**, 3813–3818 (1982).

ACKNOWLEDGMENTS

The growth of macroscopic single-crystal samples and TR-OKE measurements were supported by the U.S. Department of Energy, Office of Science–Basic Energy Sciences, grant ER46980. The PL experiments were supported by the National Science Foundation, grant DMR 1420634 (Materials Research Science and Engineering Center). S.J. acknowledges support by the Department of Energy, Office of Basic Energy Sciences, Division of Materials Sciences and Engineering, under Award DE-FG02-09ER46664, for the growth of microplate samples. We thank D. Paley for help with x-ray diffraction experiment carried out in Columbia University's Shared Materials Characterization Laboratory.

SUPPLEMENTARY MATERIALS

www.sciencemag.org/content/353/6306/1409/suppl/DC1
Materials and Methods
Table S1
Figs. S1 to S12
References (*50*, *51*)

25 April 2016; accepted 4 August 2016
10.1126/science.aaf9570

NANOMATERIALS

High-quality graphene via microwave reduction of solution-exfoliated graphene oxide

Damien Voiry,[1]*† Jieun Yang,[1]† Jacob Kupferberg,[1] Raymond Fullon,[1] Calvin Lee,[1] Hu Young Jeong,[2] Hyeon Suk Shin,[3] Manish Chhowalla[1]‡

Efficient exfoliation of graphite in solutions to obtain high-quality graphene flakes is desirable for printable electronics, catalysis, energy storage, and composites. Graphite oxide with large lateral dimensions has an exfoliation yield of ~100%, but it has not been possible to completely remove the oxygen functional groups so that the reduced form of graphene oxide (GO; reduced form: rGO) remains a highly disordered material. Here we report a simple, rapid method to reduce GO into pristine graphene using 1- to 2-second pulses of microwaves. The desirable structural properties are translated into mobility values of >1000 square centimeters per volt per second in field-effect transistors with microwave-reduced GO (MW-rGO) as the channel material and into particularly high activity for MW-rGO catalyst support toward oxygen evolution reactions.

Low yields of single-layered graphene, submicrometer lateral dimensions, and poor electronic properties remain as major challenges for solution-exfoliated graphene flakes (*1*–*4*). Oxidation of graphite and its subsequent exfoliation into monolayered graphene oxide (GO) with large lateral dimensions (*5*–*7*) produce an exfoliation yield of ~100%; however, despite numerous efforts, it has not been possible to completely remove the oxygen functional groups (*1*, *2*, *8*, *9*) so that the reduced form of GO (rGO) remains a highly disordered material with properties that are generally far inferior to graphene grown by chemical vapor deposition (CVD graphene) (*5*). Although rGO has been widely demonstrated to be a potentially useful material for catalysis (*10*–*13*) and energy storage (*14*–*18*), even in its disordered form, efficient reduction of GO into high-quality graphene should lead to substantial enhancement in performance. Here we report a simple and rapid method to reduce GO into pristine graphene by using 1- to 2-s-long microwave pulses. The microwave-reduced GO (MW-rGO) exhibits pristine CVD graphene–like features in the Raman spectrum with sharp G and 2D peaks and a nearly absent D peak. X-ray photoelectron spectroscopy (XPS) and high-resolution transmission electron microscopy (HR-TEM) suggest a highly ordered structure in which oxygen functional groups are almost entirely removed. The desirable structural properties are translated into mobility values of >1000 $cm^2 V^{-1} s^{-1}$ in field-effect transistors (FETs) with MW-rGO as the channel material and into exceptionally low Tafel slope values of ~38 mV per decade for MW-rGO catalyst support for oxygen evolution reaction (OER). These results suggest that reduction of GO using microwaves is highly efficient and realizes the goal of achieving high-quality graphene with desirable properties by solution exfoliation.

We used the modified Hummers' method to oxidize graphite and solubilize it into monolayered GO flakes in water (*19*). The stable suspension of GO sheets in water allows them be reconstituted in several different forms such as thin films (*20*), bucky paper (*21*), or fibers (*22*, *23*). GO synthesized in this manner is electrically insulating because of the presence of oxygen functional groups that are covalently bonded with the carbon atoms (*2*). Substantial effort has been devoted to recover the conducting π states of sp^2-bonded carbon atoms by removing oxygen functional groups via chemical (*1*, *24*, *25*) or thermal (*26*) reduction [even heating over 3000 K (*23*)]. By carefully tuning the reduction procedure, it is possible to realize noteworthy optical (*20*, *27*, *28*) and electronic properties (*27*) of rGO that are substantially different from those of pristine graphene because the evolution of the oxygen functional groups during reduction is accompanied by the formation of defects in the graphene basal plane (*29*). Specifically, nanoscopic holes occur through loss of carbon as CO or CO_2 (*30*), and rearrangement of the carbon atoms in the graphene basal plane leads to formation of Stone-Wales types of defects (*31*). In addition, oxygen functional groups form highly stable ether and carbonyl groups (*32*) that are difficult to remove so that rGO contains a residual oxygen concentration of 15 to 25 atomic % (at %) (*32*). These factors render rGO a highly defective material, with several studies reporting electronic mobility values on the order of 1 $cm^2 V^{-1} s^{-1}$ (*33*–*35*).

Flakes of GO with lateral dimensions as high as tens of micrometers are shown in Fig. 1A. We used microwaves from a conventional microwave oven operated at 1000 W for 1- to 2-s pulses to reduce GO [see the "Preparation of microwave-reduced graphene oxide (MW-rGO)" section in the supplementary materials] (*36*). Irradiation of GO with microwaves has been reported previously (*37*–*39*), but the reduction efficiency has been low and the rGO remains highly disordered, as indicated by the presence of an intense and broad disorder D band and the absence of the 2D band in the Raman spectra. We irradiated GO

[1]Materials Science and Engineering, Rutgers University, 607 Taylor Road, Piscataway, NJ 08854, USA. [2]Central Research Facilities and School of Materials Science and Engineering, Ulsan National Institute of Science and Technology (UNIST), Ulsan 689-798, Republic of Korea. [3]Department of Chemistry and Department of Energy Engineering, Low Dimensional Carbon Materials, UNIST, Ulsan 689-798, Republic of Korea. *Present address: Institut Européen des Membranes, University of Montpellier, Place Eugène Bataillon, 34095 Montpellier, France. †These authors contributed equally to this work. **‡Corresponding author. Email: manish1@rci.rutgers.edu**

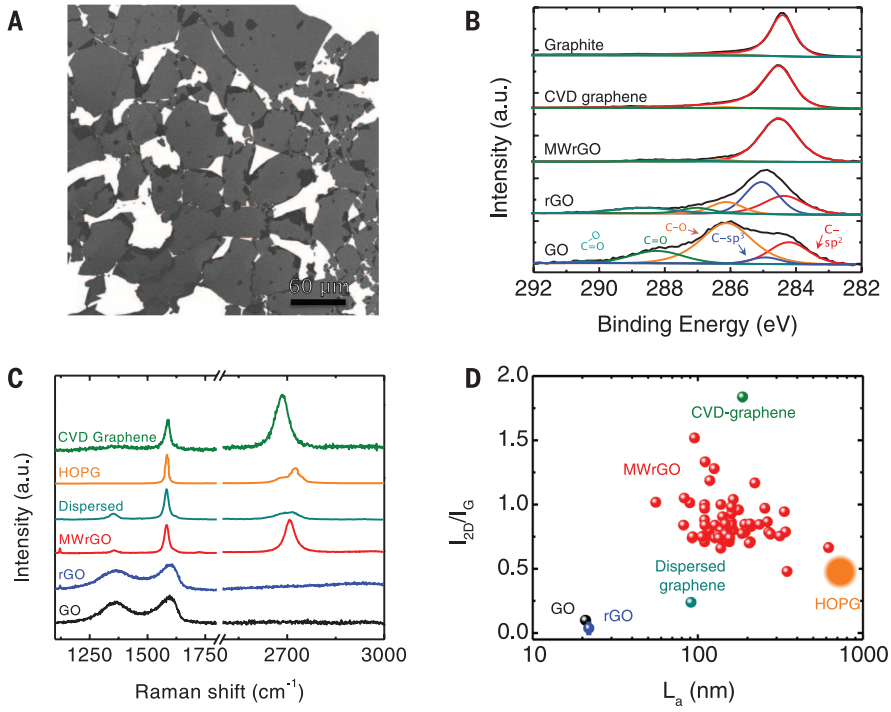

Fig. 1. Physical characterization of MW-rGO compared with pristine GO, rGO, and graphene grown by CVD. (**A**) Scanning electron microscopy of the single-layer GO flakes deposited on a silicon wafer. GO nanosheets typically have a lateral dimension of ~50 μm. (**B**) High-resolution x-ray photoelectron spectra from the C1s regions for microwaved reduced graphene oxide (MW-rGO) compared with pristine graphene oxide (GO), reduced graphene oxide (rGO), graphene grown by chemical vapor deposition (CVD graphene), and graphite. Each spectrum can be deconvoluted with components from the carbon-carbon bonds (sp^3: C–C and sp^2: C=C) as well as oxygen functional groups (C–O, C=O, and C–O=O), allowing quantification of the oxygen content. a.u., arbitrary units. (**C**) Raman spectra of MW-rGO and other graphene-based samples. The spectrum obtained for MW-rGO is similar to the spectrum of CVD graphene, with the presence of a high and symmetrical 2D band together with a minimal D band. Sharp Raman peaks indicate high crystallinity of MW-rGO and demonstrate the quality of microwave reduction. (**D**) Evolution of the I_{2D}/I_G ratio versus the crystal size (L_a) for MW-rGO, GO, rGO, highly ordered pyrolytic graphite (HOPG), dispersed graphene, and graphene from (*3*) (i.e., CVD graphene). We report 62 measurements on about five different MW-rGO samples. I_{2D}/I_G ratios and L_a values for MW-rGO are approaching those of graphene and are substantially higher than the values for rGO and dispersed graphene.

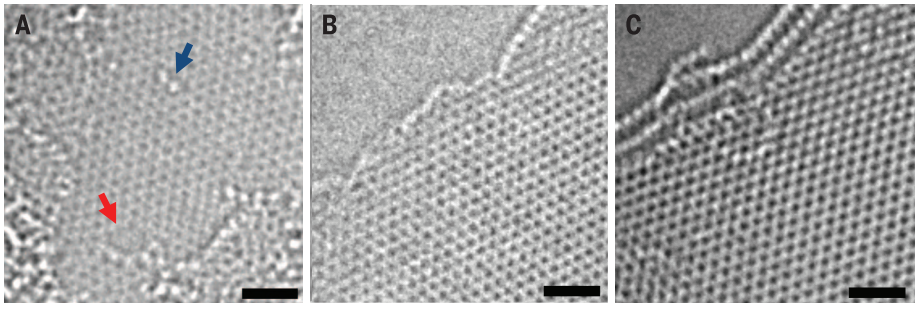

Fig. 2. High-resolution transmission electron microscopy (HR-TEM) of MW-rGO nanosheets. (**A**) HR-TEM of single-layer rGO presenting high density of defects. The red arrow denotes a hole; the blue arrow indicates an oxygen functional group. Bilayer (**B**) and trilayer (**C**) HR-TEM of MW-rGO showing highly ordered structure. Scale bars, 1 nm.

after deposition to achieve high-quality rGO. We started by slightly reducing GO by thermal annealing before exposure to microwaves, which resulted in conductive GO that could absorb microwaves. We infer that absorption of microwaves led to rapid heating of the GO (fig. S1) (*36*), causing desorption of oxygen functional groups and reordering of the graphene basal plane.

The XPS results (Fig. 1B) indicate that MW-rGO was substantially reduced with an in-plane oxygen concentration of ~4 at %, which is much lower than that theoretically predicted for rGO after annealing to 1500 K (*32*). Approximately 3 at % of noncovalently bonded adsorbed oxygen was also found in MW-rGO, CVD graphene, and graphite powder, as indicated by the fits in Fig. 1B. The full width at half maximum of the XPS peak is slightly higher in the case MW-rGO than for CVD graphene and bulk graphite, suggesting that a small amount of disorder is still present. The Raman spectra of MW-rGO, thermally reduced GO, CVD graphene, liquid-exfoliated graphene, and highly ordered pyrolytic graphite (HOPG) (for comparison) are shown in Fig. 1C. MW-rGO exhibited highly ordered graphene–like Raman features with sharp and symmetrical 2D and G peaks and a nearly absent D peak (fig. S2) (*36*). The Raman spectrum for MW-rGO (Fig. 1C) more closely resembled that of CVD graphene than the broad and highly disordered spectrum of thermally reduced rGO or that of solution-exfoliated graphene films where the 2D peak is weak and the disorder-induced D peak is also visible. The Raman spectra of MW-rGO are also different from those of electrochemically exfoliated graphene, chemically reduced GO, and microwave-exfoliated GO, all of which exhibit a high D band and a moderate or no 2D band (*25*, *37*, *40*–*42*). We have also extracted the I_{2D}/I_G Raman peak ratios (I_{2D}, intensity of the 2D peak; I_G, intensity of the G peak) as a function of the graphene domain sizes (see the "Raman spectroscopy of graphene oxide and microwaved-reduced graphene oxide" section in supplementary materials) (*36*). We found that MW-rGO exhibits substantially higher I_{2D}/I_G ratios and larger graphene domain sizes as compared with rGO and solution-exfoliated flakes (Fig. 1D).

Raman spectroscopy provides structural information averaged over regions of a few micrometers in diameter. We used aberration corrected HR-TEM to investigate local atomic structure (Fig. 2). Thermally reduced GO exhibited the well-known disordered structure with holes and oxygen functional groups on the surface (Fig. 2A). The MW-rGO exhibited highly ordered structure at the atomic scale (Fig. 2, B and C), which suggests that there is some reorganization of the carbon bonding during microwave reduction, along with removal of oxygen facilitated by achieving exceptionally high temperatures.

To investigate whether the highly ordered structure of MW-rGO can be translated into useful properties, we implemented it as the channel in FETs and as a catalyst support for the OER. The mobility values in graphene have been used as a parameter for assessing the quality of the material (*43*). To this end, several studies have reported high mobility values for rGO (100 to 1000 $cm^2 V^{-1} s^{-1}$) (*40*, *42*) to demonstrate efficacy of various reduction treatments or synthesis procedures. However, mobility values alone cannot provide information about the structural integrity of the material. Previous reports on high-mobility rGO are accompanied by Raman spectra containing large D bands and weak 2D bands, along with oxygen concentrations of 5 to 8%,

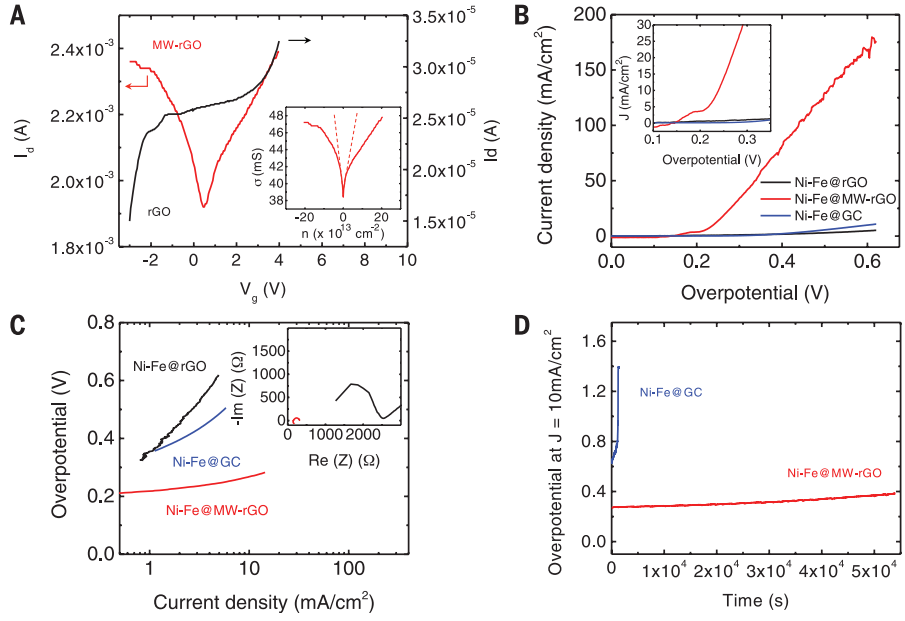

Fig. 3. Characterization of the electronic and electrocatalytic properties of MW-rGO. (**A**) Transfer characteristics of MW-rGO and rGO measured at drain voltage (V_{ds}) = 50 mV. MW-rGO displays ambipolar behavior with a Dirac cone at gate voltage (V_g) ~ 0.5 V. I_d, drain current. (Inset) Evolution of the MW-rGO conductivity with the carrier density. n, carrier concentration; σ, conductivity. (**B**) Polarization curves obtained from Ni-Fe layered double hydroxide (LDH) deposited on MW-rGO (Ni-Fe@MW-rGO), rGO (Ni-Fe@rGO), and glassy carbon (Ni-Fe@GC). (Inset) Magnification of the onset potential. J, current density. (**C**) Tafel plot of Ni-Fe LDH deposited on MW-rGO compared with GC and rGO. (Inset) Nyquist plots of the different samples obtained by electrochemical impedance spectroscopy at η = 200 mV. Ni-Fe@MW-rGO clearly shows a reduced internal resistance and minimal charge transfer resistance that can be attributed to the high conductivity of the MW-rGO nanosheets. Re (Z), real part of the impedance; -Im (Z), imaginary part of the impedance. (**D**) Galvanostatic measurements showing the electrocatalytic stability of Ni-Fe LDH deposited on glassy carbon and MW-rGO when driving a 10 mA/cm^2 current density over 15 hours. The MW-rGO support shows the best stability with minimal change of the overpotential. Contrastingly, the activity from the Ni-Fe LDH on glassy carbon decreases rapidly.

suggesting substantial disorder. Thus, mobility values >~1 cm^2 V^{-1} s^{-1} have not been widely reproducible in rGO. Transfer characteristics of FETs from MW-rGO on SiO_2 [see Materials and methods section for device-fabrication procedure (*36*)] are shown in Fig. 3A. Drain currents can be measured in the milliamp range. The electrical properties of thermally reduced GO FETs are also shown for comparison (Fig. 3A); these FETs exhibit substantially lower current values. In the case of rGO, the absence of a Dirac point is attributed to the poorly reduced and highly disordered structure of the nanosheets. Additionally, the presence of adsorbates and oxygen impurities is known to dramatically shift the position of the Dirac point and to modify the FET characteristics. The mobility values extracted from FET measurements were >1000 cm^2 V^{-1} s^{-1} for holes and electrons in MW-rGO (Fig. 3A, inset, and fig. S4) (*36*). FETs measured here consist of large channel dimensions so that the transport of carriers occurs over numerous flakes. Despite this, exceptionally high mobility values were obtained in MW-rGO, suggesting that individual flakes have very good transport properties. Although we obtain exceptional mobilities, they should be interpreted with caution as the actual values can be strongly influenced by extrinsic factors such as contact resistance and scattering by charged impurities (*44*).

Highly conducting carbon-based electrodes that are electrochemically stable are important for applications in catalysis and energy storage. Catalysts are typically loaded on highly conducting substrates (working electrodes) such as carbon cloth, glassy carbon, or nickel foam. We investigated the properties of MW-rGO as a catalyst support in OER by depositing Fe and Ni layered double hydroxide (LDH) on MW-rGO [see Materials and methods section (*36*)]. The OER properties of Fe-Ni LDH catalysts on MW-rGO, rGO, and glassy carbon electrodes (Fig. 3B) [see Materials and methods section for the electrochemical measurements (*36*)] show that the overpotential at which the reaction starts decreased to <200 mV and the current density rapidly increased when MW-rGO was used as the catalyst support. To obtain insight into surface chemistry mechanisms, we have extracted the Tafel slopes from measurements on different supports (Fig. 3C). The MW-rGO catalyst supports exhibit very low Tafel slopes of 38 mV per decade, which may indicate that the reaction $MO + OH^- = MOOH + e^-$ (where M represents an active site on the catalyst surface and e^- represents an electron) is the rate-determining step (*45*). The much higher Tafel slopes for glassy carbon and rGO electrodes of 170 mV per decade and 360 mV per decade, respectively, suggest that limiting reactions are caused by adsorption of hydroxide ions ($M + OH^- = MOH + e^-$) because of the poor electrical coupling between the catalyst and the support (*45*). The limited electrical coupling is highlighted by the inset in Fig. 3C, which shows that the impedance of the electrochemical circuit is substantially lowered when using MW-rGO, which allows the OER to proceed efficiently. Electrochemical stability of the catalysts and their supports is an important parameter in catalysis. The stability of MW-rGO supports (Fig. 3D) was maintained for more than 15 hours, in contrast with glassy carbon supports that degraded almost immediately after the reaction started. We have made similar measurements for the hydrogen evolution reaction and obtained desirable performance for MW-rGO catalyst supports, as well as very high stability for more than 100 hours [see the "Hydrogen evolution reaction (HER)" section in supplementary materials] (*36*).

REFERENCES AND NOTES

1. S. Park, R. S. Ruoff, *Nat. Nanotechnol.* **4**, 217–224 (2009).
2. K. P. Loh, Q. Bao, P. K. Ang, J. Yang, *J. Mater. Chem.* **20**, 2277–2289 (2010).
3. K. R. Paton *et al.*, *Nat. Mater.* **13**, 624–630 (2014).
4. K. P. Loh, Q. Bao, G. Eda, M. Chhowalla, *Nat. Chem.* **2**, 1015–1024 (2010).
5. C.-Y. Su *et al.*, *Chem. Mater.* **21**, 5674–5680 (2009).
6. J. Zhao, S. Pei, W. Ren, L. Gao, H.-M. Cheng, *ACS Nano* **4**, 5245–5252 (2010).
7. Q. Zheng *et al.*, *ACS Nano* **5**, 6039–6051 (2011).
8. I. Jung, D. A. Dikin, R. D. Piner, R. S. Ruoff, *Nano Lett.* **8**, 4283–4287 (2008).
9. K. Erickson *et al.*, *Adv. Mater.* **22**, 4467–4472 (2010).
10. E. Yoo *et al.*, *Nano Lett.* **9**, 2255–2259 (2009).
11. Y. Liang *et al.*, *Nat. Mater.* **10**, 780–786 (2011).
12. Y. Li *et al.*, *J. Am. Chem. Soc.* **133**, 7296–7299 (2011).
13. J. Yang *et al.*, *Angew. Chem. Int. Ed.* **52**, 13751–13754 (2013).
14. M. D. Stoller, S. Park, Y. Zhu, J. An, R. S. Ruoff, *Nano Lett.* **8**, 3498–3502 (2008).
15. J. G. Radich, P. V. Kamat, *ACS Catal.* **2**, 807–816 (2012).
16. H. Wang *et al.*, *J. Am. Chem. Soc.* **132**, 13978–13980 (2010).
17. H. Wang *et al.*, *Nano Lett.* **11**, 2644–2647 (2011).
18. G. Yu *et al.*, *Nano Lett.* **11**, 2905–2911 (2011).
19. W. S. Hummers Jr., R. E. Offeman, *J. Am. Chem. Soc.* **80**, 1339 (1958).
20. G. Eda, G. Fanchini, M. Chhowalla, *Nat. Nanotechnol.* **3**, 270–274 (2008).
21. D. A. Dikin *et al.*, *Nature* **448**, 457–460 (2007).
22. R. Cruz-Silva *et al.*, *ACS Nano* **8**, 5959–5967 (2014).
23. G. Xin *et al.*, *Science* **349**, 1083–1087 (2015).
24. S. Park *et al.*, *Nat. Commun.* **3**, 638 (2012).
25. I. K. Moon, J. Lee, R. S. Ruoff, H. Lee, *Nat. Commun.* **1**, 73 (2010).
26. X. Li *et al.*, *Nat. Nanotechnol.* **3**, 538–542 (2008).
27. G. Eda *et al.*, *Adv. Mater.* **22**, 505–509 (2010).
28. Z. Luo, P. M. Vora, E. J. Mele, A. T. C. Johnson, J. M. Kikkawa, *Appl. Phys. Lett.* **94**, 111909 (2009).
29. D. R. Dreyer, S. Park, C. W. Bielawski, R. S. Ruoff, *Chem. Soc. Rev.* **39**, 228–240 (2010).
30. R. Larciprete *et al.*, *J. Am. Chem. Soc.* **133**, 17315–17321 (2011).
31. J. Kotakoski, A. V. Krasheninnikov, K. Nordlund, *Phys. Rev. B* **74**, 245420 (2006).
32. A. Bagri *et al.*, *Nat. Chem.* **2**, 581–587 (2010).
33. Z. Luo, Y. Lu, L. A. Somers, A. T. C. Johnson, *J. Am. Chem. Soc.* **131**, 898–899 (2009).
34. H. A. Becerril *et al.*, *ACS Nano* **2**, 463–470 (2008).
35. S. Wang *et al.*, *Nano Lett.* **10**, 92–98 (2010).
36. See supplementary materials on *Science* Online.

37. Y. Zhu *et al.*, *Carbon* **48**, 2118–2122 (2010).
38. W. Chen, L. Yan, P. R. Bangal, *Carbon* **48**, 1146–1152 (2010).
39. H. Hu, Z. Zhao, Q. Zhou, Y. Gogotsi, J. Qiu, *Carbon* **50**, 3267–3273 (2012).
40. H. Feng, R. Cheng, X. Zhao, X. Duan, J. Li, *Nat. Commun.* **4**, 1539 (2013).
41. K. Parvez *et al.*, *J. Am. Chem. Soc.* **136**, 6083–6091 (2014).
42. S. Eigler *et al.*, *Adv. Mater.* **25**, 3583–3587 (2013).
43. N. Petrone *et al.*, *Nano Lett.* **12**, 2751–2756 (2012).
44. I. McCulloch, A. Salleo, M. Chabinyc, *Science* **352**, 1521–1522 (2016).
45. T. Shinagawa, A. T. Garcia-Esparza, K. Takanabe, *Sci. Rep.* **5**, 13801 (2015).

ACKNOWLEDGMENTS

M.C. and D.V. acknowledge financial support from NSF Division of Graduate Education (grant 0903661) and Electrical, Communications and Cyber Systems (grant 1128335). J.Y., J.K., and M.C. acknowledge financial support from the Rutgers Energy Institute. R.F. acknowledges financial support from the U.S. Department of Education Graduate Assistance in Areas of National Need program (grant P200A120142). C.L. and J.K. acknowledge support from the Rutgers ARESTY Research Assistant program. H.S.S. acknowledges support from the National Research Foundation (NRF) (grant NRF 2014R1A2A2A01007136) and from the Center for Advanced Soft Electronics (grant code 2011-0031630) under the Global Frontier Research Program through the NRF funded by the Ministry of Science, ICT and Future Planning, Korea. All data are in the main paper and the supplementary materials.

SUPPLEMENTARY MATERIALS

www.sciencemag.org/content/353/6306/1413/suppl/DC1
Materials and Methods
Supplementary Text
Figs. S1 to S6
Table S1
References (*46*–*57*)

12 June 2016; accepted 23 August 2016
Published online 1 September 2016
10.1126/science.aah3398

GEOPHYSICS

Surface uplift and time-dependent seismic hazard due to fluid injection in eastern Texas

Manoochehr Shirzaei,[1]* William L. Ellsworth,[2] Kristy F. Tiampo,[3]† Pablo J. González,[4]‡ Michael Manga[5]

Observations that unequivocally link seismicity and wastewater injection are scarce. Here we show that wastewater injection in eastern Texas causes uplift, detectable in radar interferometric data up to >8 kilometers from the wells. Using measurements of uplift, reported injection data, and a poroelastic model, we computed the crustal strain and pore pressure. We infer that an increase of >1 megapascal in pore pressure in rocks with low compressibility triggers earthquakes, including the 4.8–moment magnitude event that occurred on 17 May 2012, the largest earthquake recorded in eastern Texas. Seismic activity increased even while injection rates declined, owing to diffusion of pore pressure from earlier periods with higher injection rates. Induced seismicity potential is suppressed where tight confining formations prevent pore pressure from propagating into crystalline basement rocks.

In recent years, the eastern and central United States have experienced a sharp increase in the number of earthquakes, with more than 1570 events with moment magnitudes (M_w) ≥ 3 between 2009 and 2015 (*1*–*3*). Many of these events occurred near injection disposal wells and were preceded by a high rate of fluid injection over a period of months to years, suggesting a link between seismicity and injection operations (*1*, *3*–*8*). In general, earthquake hazard is proportional to the seismic rate; thus, the current increase in the seismic rate implies an elevated hazard in the central and eastern United States (*9*).

On 17 May 2012, the city of Timpson, Texas, experienced a M_w 4.8 earthquake, the largest recorded event in the region (Fig. 1A). This event was preceded and followed by several earthquakes located on an inferred northwest-southeast–trending basement fault, including three with M_w ≥ 4.0 over the following 16 months. Focal depths were shallow, ranging from 1.6 to 5.0 km, with the majority of the strain released between 3.5 and 5 km (*5*). Four high-volume class II disposal wells are located within ~10 km, and two lie directly above the site of the earthquakes (table S1). They dispose coproduced saline formation water from oil and gas production operations in the area by injecting into Lower Cretaceous limestones within the Sabine Uplift of eastern Texas (*10*). There are other injection wells in the vicinity, but none is closer than 7 km to the four studied wells (table S8 and fig. S8) or is a high-volume injector. The immediate area near the disposal wells and the earthquakes has limited oil and gas production. The four disposal wells began injection between 2005 and 2007 at a net average rate of 890,000 m^3/year until mid-2012, when injection dropped to 720,000 m^3/year (*5*).

The proximity of the earthquake clusters to the injection wells suggests a link between them (*5*, *11*). As wastewater is injected into the disposal formation, it increases pore pressure within the connected hydrogeologic system. Over time, the pressure perturbation can spread to distances of many kilometers (*12*, *13*). The increase in pore pressure caused by the injection of fluids decreases the effective normal stress on faults, bringing them closer to failure (*14*–*16*), as well as locally changing differential stress within the reservoir and surrounding rocks (*17*–*19*). Moreover, increased pore pressure can cause surface deformation (*19*), measurable using geodetic tools (*20*), which provides the possibility of documenting subsurface evolution from the surface. Among geodetic tools, interferometric synthetic aperture radar (InSAR) and the Global Positioning System (GPS) have been widely used to monitor surface deformation resulting from natural and anthropogenic processes.

We applied a multitemporal InSAR approach (*21*) to three overlapping sets of L-band SAR images (tables S2 and S3) acquired by the Advanced Land Observing Satellite (ALOS) over the Timpson area between 6 May 2007 and 14 November 2010 (Fig. 1A). High-quality interferograms were generated from these L-band data (fig. S1). We improved the signal-to-noise ratio of the measurements by estimating the linear velocity from time series obtained by inverting a large number of interferograms (*22*). Using velocity maps for each individual data set and the combined map (*22*), we found a line-of-sight (LOS) uplift rate of up to 3 mm/year over the area between the injection wells (Fig. 1B). We estimated that the rate of volume increase under the LOS velocity surface is 800,000 to 1,000,000 m^3/year, assuming an elastic material with a Poisson's ratio of 0.25 to 0.33 estimated from seismic velocities profiles, which is consistent with the net injected volume rate at the injection wells. To validate ALOS observations and evaluate the current state of ground deformation, we also applied the same processing scheme to eight C-band images acquired by the RADARSAT-2 satellite between 6 March and 21 August 2014 (fig. S2 and tables S4 and S5). Although the location of the zone of maximum deformation is consistent with the velocity map obtained from the L-band data, its spatial extent is broader, with a maximum uplift of ~5 mm over a ~6-month interval.

The two western wells (W1 and W2) inject (Fig. 1C) at a depth of 1800 m into Trinity Group

[1]School of Earth and Space Exploration, Arizona State University, Tempe, AZ 85287, USA. [2]Department of Geophysics, Stanford University, Stanford, CA 94305, USA. [3]Department of Earth Sciences, University of Western Ontario, London, Ontario, Canada. [4]Centre for the Observation and Modelling of Earthquakes, Volcanoes and Tectonics (COMET) and Institute of Geophysics and Tectonics, School of Earth and Environment, University of Leeds, Leeds LS2 9JT, UK. [5]Department of Earth and Planetary Science, University of California, Berkeley, CA 94709, USA.
***Corresponding author. Email: shirzaei@asu.edu** †Present address: Cooperative Institute for Research in Environmental Sciences and Department of Geological Sciences, UCB 216, University of Colorado, Boulder, CO 80309, USA. ‡Present address: COMET and Liverpool Earth Observatory, Department of Earth, Ocean and Ecological Sciences, University of Liverpool, Liverpool L69 3GP, UK.

High-quality graphene via microwave reduction of solution-exfoliated graphene oxide

Damien Voiry, Jieun Yang, Jacob Kupferberg, Raymond Fullon, Calvin Lee, Hu Young Jeong, Hyeon Suk Shin and Manish Chhowalla

Science **353** (6306), 1413-1416.
DOI: 10.1126/science.aah3398originally published online September 1, 2016